Hydrogen-induced insulating state accompanied by interlayer charge ordering in $SmNiO_3$

Kunihiko Yamauchi* and Ikutaro Hamada

Department of Precision Engineering, Graduate School of Engineering, Osaka University, Suita, Osaka 565-0871, Japan

(Received 14 October 2022; revised 9 June 2023; accepted 21 June 2023; published 6 July 2023)

The effect of hydrogen doping on the crystal structure and the electronic state of $SmNiO_3$ is investigated by means of density functional theory with a combinatorial structure-generation approach. While 100% of hydrogen doping per Ni atom has been supposed to be responsible for the experimentally observed insulating phase, we found that 50% of hydrogen doping results in an outstandingly stable atomic structure showing the insulating property after the structural relaxation was performed while imposing a ferromagnetic configuration. The stable crystal structure shows the peculiar layered pattern of charge disproportionation of Ni^{2+} and Ni^{3+} valences together with the strong Jahn-Teller distortion that causes the e_g orbital state splitting and opens the band gap.

DOI: 10.1103/PhysRevB.108.045108

I. INTRODUCTION

Transition-metal oxides represented by ABO_3-type perovskite show intriguing phenomena as functional materials for ferroelectric, magnetic, catalytic, and electrochemical applications. Among them, rare-earth nickelates $RNiO_3$ (R = rare-earth element) attract a lot of attention for their peculiar metal-insulator transition, triggered by the unstable formal oxidation state of Ni^{3+} cations that split into Ni^{2+} and Ni^{4+} in the low-temperature phase [1–7]. One possible application of nickelates related to the metal-insulator transition is a nanoscale resistive switching device, termed a memristor, that has recently generated huge interest in its use in neuromorphic applications [8,9]. There is also a potential for other device applications such as photonic devices and colossal magnetoresistance devices [10].

Recently, it was shown that chemical doping can be used to drive the phase change in $SmNiO_3$ thin films [9,11–13]. There, it was demonstrated that the electronic conductivity is decreased by more than eight orders of magnitude by doping hydrogen. It was proposed that additional electrons donated by H atoms change the ionic valence of Ni from Ni^{3+} to Ni^{2+} and cause the Mott transition. Similarly, Li and Mg ion doping was found to lead to the transition and suppression of electronic transport [14]. From the theoretical side, Yoo and Liao recently introduced H and Li atoms into $SmNiO_3$ in a density functional theory (DFT) simulation with the Hubbard U correction and observed a metallic state at low H concentrations and the transition to an insulating phase at a high H concentration (Ni:H ratio of 1) with a band gap of 3.0 eV in the ferromagnetic configuration [15]. The trend of the chemical-doping-induced Mott transition in the $RNiO_3$ series was further investigated [16,17]. A similar DFT simulation was performed by Kotiuga and Rabe [18]; they tracked the change in the electronic structure by adding electrons compensated by a uniform positive background charge and found a wide-gap insulating phase at 100% doping, which is consistent with Yoo and Liao's study. Several magnetic configurations have also been considered.

In this study, we investigate the H-doping effect in $SmNiO_3$ using a DFT simulation, focusing on the doping-induced low-symmetry structural distortion and the consequent change in the electronic state. Especially, the microscopic origin of the doping-induced insulating phase and its relation to charge ordering are examined with particular attention to uncover the role of hydrogen placed in a transition-metal oxide. To this end, detailed information about the crystal structure and occupation sites of doped H atoms is necessary. In particular, it is vital to understand how the crystal structure and the associated electronic structure evolve as the hydrogen concentration increases. Hence, we perform an exhaustive simulation for H-doped $SmNiO_3$ considering all the H atom arrangements in a supercell.

II. STRUCTURAL AND COMPUTATIONAL DETAILS

The high-temperature (HT) phase of $RNiO_3$ shows the orthorhombic $Pbnm$ crystal structure (nonstandard setting of $Pnma$) in which the c axis is the longest one and the ab plane lies parallel to the NiO layer [Fig. 1(a)]. With respect to an ideal cubic perovskite, $GdFeO_3$-type octahedral tilting and the cooperative Jahn-Teller (JT) distortion lower the symmetry. The low-temperature (LT) phase shows the monoclinic $P2_1/n$ structure, as shown in Fig. 1(b) [19]. In this structure, the JT distortion is suppressed, while the Ni-O bond disproportionation and the breathing-mode distortion of NiO_6 octahedra create two nonequivalent Ni sites (Ni^{2+} and Ni^{4+}) in the insulating phase. While the LT structure exhibits a total energy 13 meV lower than that in the HT structure, we hereinafter focus on the high-symmetry HT structure. Room-temperature $SmNiO_3$ in a thin-film form shows bad-metallic conductivity in which disorder and consequent atomic distortions seem to compensate the charge disproportionation and increase the electric conductivity [20]. Since we aim to simulate a metal-insulator transition induced purely by hydrogen doping, not by temperature or the disorder effect, we consider a phase transition from a metallic phase with

*Present address: Center for Spintronics Research Network, Osaka University, Toyonaka, Osaka 560-8531, Japan; yamauchi.kunihiko.es@osaka-u.ac.jp

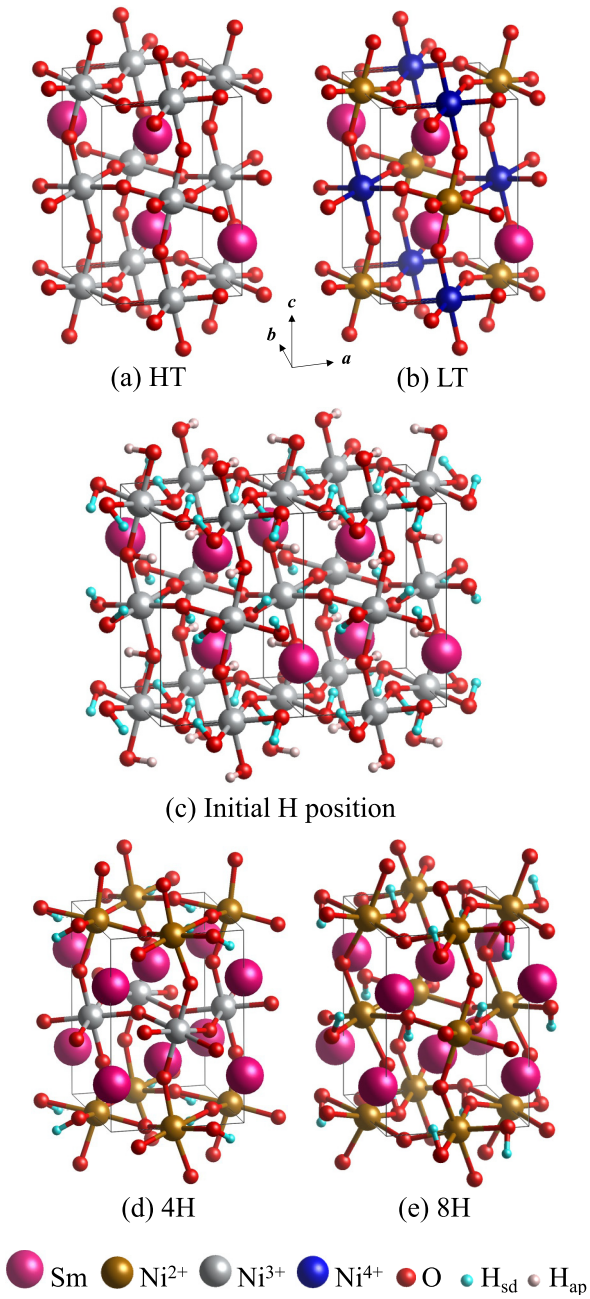

FIG. 1. (a) HT *Pbnm* and (b) LT $P2_1/n$ crystal structures of $SmNiO_3$. (c) Initial H atom positions used in all the H-doping simulations in a $2 \times 1 \times 1$ supercell of *Pbnm* $SmNiO_3$. The 16 side H (H_{sd}) and 8 apical H (H_{ap}) sites are shown in different colors. According to the doping concentration, some of the H sites were chosen to be occupied, and other sites were left unoccupied in generating the initial H_x-$SmNiO_3$ crystal structures. (d) The 4H *Pb* structure of $H_{0.5}$-$SmNiO_3$ and (e) 8H $P2_12_12_1$ structure of $H_{1.0}$-$SmNiO_3$ predicted to be the most stable.

the high-symmetry HT structure to insulating phases with low-symmetry structures distorted by the hydrogen doping. This concept is similar to that in a previous DFT study [15], but we extend the simulation to a larger supercell to explore a large configurational space. As reported in previous studies [15,21], the most preferential site for a single

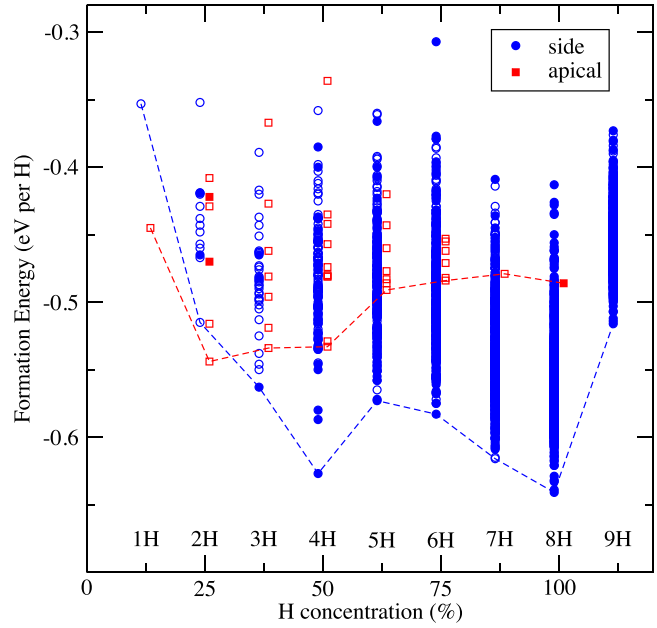

FIG. 2. Formation energy of H_x-$SmNiO_3$ as a function of H doping concentration per Ni for side doping and apical doping. Open and solid symbols denote metallic and insulator states, respectively.

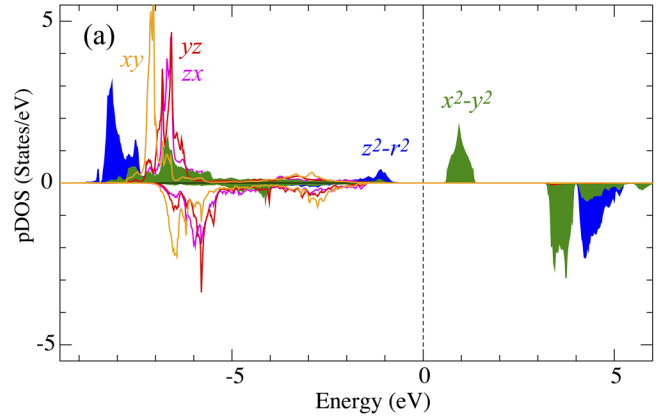

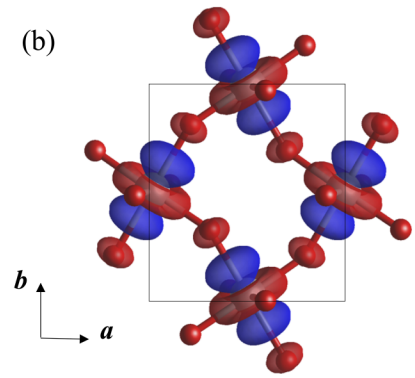

FIG. 3. (a) Projected DOS of the Ni $3d$ state at the Ni^{3+} site in 4H structure of $H_{0.5}$-$SmNiO_3$ using the HSE06 exchange-correlation functional. (b) MLWF contour plot of the occupied Ni e_g state in the $Ni^{3+}O_2$ layer.

TABLE I. The optimized lattice parameters, cell volume, and distortion modes and their amplitudes (in Å) for the HT (*Pbnm*) and LT ($P2_1/n$) structures of $SmNiO_3$, 4H (*Pb*) structure of $H_{0.5}$-$SmNiO_3$, and 8H ($P2_12_12_1$) structure of $H_{1.0}$-$SmNiO_3$ with respect to the ideal cubic perovskite structure ($Pm\bar{3}m$). Only displacive modes with amplitudes larger than 0.1 Å are listed. The Γ mode is not listed for simplicity. An asterisk symbol (∗) denotes an out-of-phase mode, while the others are in-phase modes.

	HT	LT	4H	8H	Mode
Lattice constants (Å)					
a	5.262	5.279	5.230	5.386	
b	5.460	5.429	5.737	6.010	
c	7.512	7.518	7.553	7.512	
Monoclinic angle α (deg)	90.00	90.00	90.53	90.00	
Cell volume V (Å^3/2 f.u.)	215.87	215.11	226.68	243.25	
X_1^+			0.21		interlayer breathing
X_5^+	0.67	0.65	0.93	1.13	a^+ tilting
X_5^-			0.14	0.26	bending*
M_2^+	0.01	0.01	0.08	0.07	JT
M_2^-				0.25	Sm c displacement
M_3^+	0.97	0.96	1.36	1.29	c^+ tilting
M_3^-				0.16	O^{ap} c displacement
M_5^-			0.19		O^{ap}, Ni off centering
R_1^+		0.13			breathing*
R_3^+		0.00	0.23		JT*
R_4^+	1.35	1.31	1.42	1.93	b^+ tilting*
R_4^-			0.20	0.39	Ni off centering*
R_5^+	0.17	0.14	0.22	0.42	bending*

H atom is an interstitial site in the (001) planes near the edges of a NiO_6 octahedron with an O-H bond to the side oxygen (we will call it "side doping" hereafter). Another stable site is found in the (001) plane with the O-H bond to the apical oxygen ("apical doping"), as shown in Fig. 1(c). To systematically investigate the spatial distribution of doped H atoms, we constructed a $2 \times 1 \times 1$ *Pbnm* supercell with 8 f.u. containing 16 side O and 8 apical O atoms [Fig. 1(c)], and all the possible H patterns were considered by a combinatorial structure-generation approach using the SUPERCELL [22] program by increasing the number of the doped H atoms from 1 to 9. This yields the number of combinations, which explosively increase as ${}_nC_m$ to select m out of n sites: ${}_{16}C_1 = 16$, ${}_{16}C_2 = 120$, ${}_{16}C_3 = 560, \ldots,$ ${}_{16}C_8 = 12\,870$, reaching a maximum at half doping. However, these numbers can be reduced to $\sim 1/16$ by taking into account the 16 symmetry operations in the *Pbnm* space group. We thus generated 1, 13, 35, 134, 273, 539, 715, 854, and 715 (3279 total) structures for the side doping ($n = 16$ and $m = 1$ to 9) and 1, 6, 7, 13, 7, 6, 1, and 1 (42 total) structures for the apical doping ($n = 8$ and $m = 1$ to 8).

To evaluate the structural stability, we used the projector augmented wave method [23] as implemented in the VASP code [24]. The Perdew-Burke-Ernzerhof (PBE) [25] generalized gradient approximation was used for the exchange-correlation and the Hubbard-U correction [26] (PBE+U), with an effective U of 3 eV applied to the Ni $3d$ state. Atomic positions and lattice parameters were fully optimized for each H atomic configuration. After the full geometry optimization of the atomic positions and the lattice parameters, the total energy was evaluated by using the tetrahedron method with Blöchl corrections [27] with $2 \times 4 \times 3$ $\boldsymbol{k}$-mesh points. During the structural optimization, H atoms freely move around but retain the bond to O atoms. The spin configuration was set in the ferromagnetic state to prevent a symmetry reduction. If some antiferromagnetic (AFM) configuration is set, the system often encounters a mismatch between the AFM pattern and CO pattern, resulting in an unstable state. Additional information on the magnetic stability can be found in the Supplemental Material [28]. To characterize the H-induced structural distortion in $SmNiO_3$, the crystalline symmetry and structural distortion modes were investigated by using ISOCIF and ISODISTORT programs [29,30]. The crystallographic figures were generated using the VESTA program [31].

III. STRUCTURAL STABILITY UNDER HYDROGEN DOPING

Figure 2 shows the calculated formation energy (per H atom), defined as $E_f = E(H_x\text{-}SmNiO_3) - E(SmNiO_3) - \frac{x}{2}E(H_2)$, as a function of the H-doping concentration x. The three terms on the right-hand side of the above equation denote the total energies of hydrogen-doped $SmNiO_3$, pristine $SmNiO_3$, and a H_2 molecule, respectively. The apical doping has lower energy at low doping ($\leqslant$25%), while the side doping has lower energy at high doping ($\geqslant$27.5%). The global energy minimum is located at 100% (H:Ni = 1:1) doping, at which the most stable structure has a formation energy of −0.64 eV/H. The ratio of insulating structures (those with a finite band gap) increases as the H concentration increases. At 100% H doping, all 854 structures are in the insulating

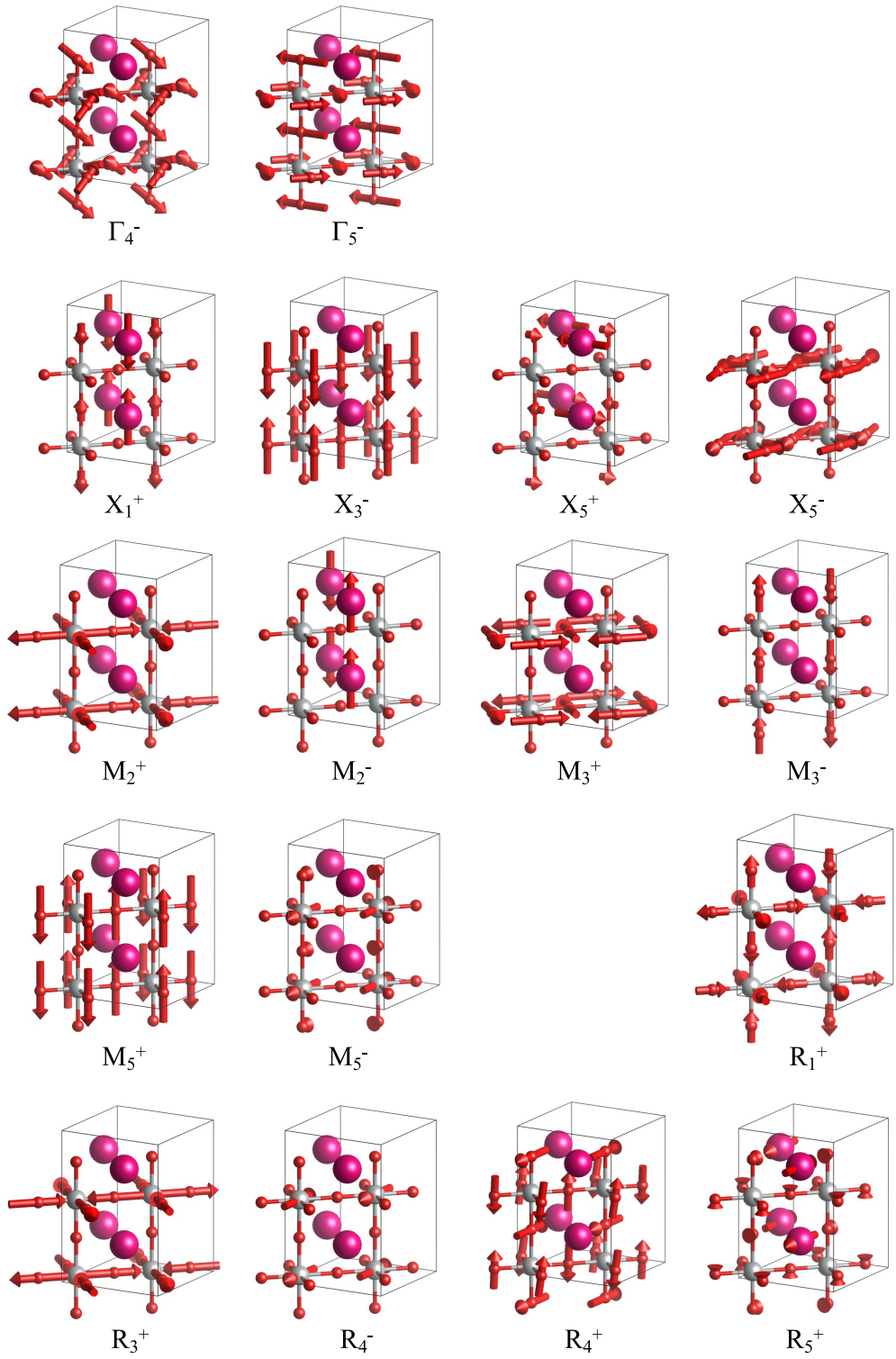

FIG. 4. Distortion modes for the $\sqrt{2} \times \sqrt{2} \times 2$ $SmNiO_3$ supercell with respect to the ideal cubic perovskite structure ($Pm\bar{3}m$). The mode names correspond to Table I.

state. In the overdoping state (>100%), the system becomes unstable again since the Ni ion favors divalent or trivalent states but not the monovalent state. Unexpectedly, a prominent local minimum appears at 50% H doping, at which the most stable structure has a formation energy of −0.63 eV/H, more than 0.04 eV/H lower than the second most stable structure. Hereinafter, the stable structures are referred to as "8H" and "4H," and we will focus on their structural and electronic properties since these structures may be responsible for the experimentally observed insulating phase.

Our symmetry analysis revealed that the 8H structure has the chiral $P2_12_12_1$ space group and the primitive cell is

reduced to a half cell (4 f.u.), as shown in Fig. 1(e). Remarkably, the structure has only one equivalent site for Ni and Sm atoms and three for O atoms. Each NiO_6 octahedron bonds with two H atoms that provide one electron to one Ni atom, consistent with what was reported in a previous DFT study [15]. By comparing the present structure and that in the literature, we found that the our structure has higher symmetry (the previous one has $P1$ symmetry) and much lower energy (by 5 meV/f.u.) after optimizing both structures. This finding of the high-symmetry structure demonstrates the superiority of the computational approach exhaustively taking into account all the doped H atom configurations. The band gap is calculated to be 1.41 eV with the PBE + U method. By using the Heyd-Scuseria-Ernzerhof (HSE06) screened hybrid functional method [32], the calculated band gap increases to 5.12 eV.

To our surprise, we found that the 4H structure of $H_{0.5}$-$SmNiO_3$ also has a highly symmetric structure in the 4 f.u. cell with Pb symmetry, as shown in Fig. 1(d). There are two equivalent Ni sites, namely, Ni^{2+} and Ni^{3+}, showing a layered charge-ordering pattern forming a $Ni^{2+}O_2$ layer and a $Ni^{3+}O_2$ layer alternatively. These ionic valences can be distinguished at a glance by the calculated spin momenta: $S(Ni^{2+}) = 1.5\mu_B$ and $S(Ni^{3+}) = 1.0\mu_B$. In the $Ni^{2+}O_2$ layer, one additional electron is provided by an H atom to the Ni site, making the e_g state fully occupied in one spin channel. In the $Ni^{3+}O_2$ layer, Ni ions stay in a trivalent state, while the NiO_6 octahedral tilting and JT distortion are enhanced by H doping. This results in the large energy splitting of the e_g state shown in Fig. 3(a); here the density of states (DOS) is projected onto the Ni $3d$ orbital state under an O_h crystal field using maximally-localized Wannier functions (MLWFs) [33–35]. The band gap is evaluated to be 0.36 and 1.4 eV by the PBE+U and HSE06 methods, respectively. In Fig. 3(b), the orbital ordering can be seen in the $Ni^{3+}O_2$ layer; the alternating "$x^2 - r^2/y^2 - r^2$ orbital ordering pattern" of the occupied $z^2 - r^2$ state looks similar to that caused by cooperative JT distortion in $RMnO_3$ [36,37]. Making a keen contrast to other perovskite transition-metal oxides, the unusual interlayer charge ordering and the intralayer orbital ordering coexist in the 4H structure.

Table I shows the amplitude of the distortion modes of the HT, LT, 4H, and 8H structures with respect to the cubic perovskite structure. The ionic displacement for each mode is illustrated in the Appendix. In the HT structure, the octahedron-tilting X_5^+, M_3^+, and R_4^+ modes are dominant. The H atom that bonds to the side O atom enhances the octahedron-tilting modes and bending modes in 4H and 8H structures. The R_3^+ mode shows a large amplitude in the 4H structure, leading to the out-of-phase JT distortion. These unusual distortion modes are supported by the lattice expansion due to interstitial H doping. In the 4H structure, since H atoms are positioned to form stripes along the b axis, the lattice is expanded along the b direction. This uniaxial strain in turn supports the R_3^+ mode softening. To highlight the effect, we carried out H-doping simulations in $SmNiO_3$ in which lattice parameters were fixed to those of a nondoped structure. This resulted in a monotonous behavior of the formation energy with respect to the H concentration, and the energy minima at the 4H and 8H structures disappeared (see the Supplemental Material [28]); the R_3^+ distortion in the 4H structure decreased the amplitude from 0.23 to 0.07 Å in the fixed lattice calculation. Therefore, H doping in nickelate exhibits two important ingredients for the phase transition: low-symmetry ionic distortions and lattice expansion that, in turn, promotes the JT distortion in the $Ni^{3+}O_2$ layer.

IV. SUMMARY

By means of combinatorial DFT calculations, we examined the total energy of more than 3000 structures in H-doped $SmNiO_3$ and found a very stable structure at 50% H concentration manifesting an unusual layered pattern of charge ordering in the insulating state. While our simulation results may provide a reasonable explanation for the experimentally observed insulating state, the realistic magnetic order at room temperature is likely the paramagnetic one [38], and the difference from the ferromagnetic configuration that we considered in the DFT calculation may lead to the different structural stability. Further experimental studies and structural analysis with quantification of the H doping concentration are needed to confirm our findings. This study also demonstrated that combinatorial structural generation can be a fine tool for finding stable structures under chemical doping, thus providing a reference for future research in the field of hydrogen-doped oxides, in which a significant change in the electronic structure caused by structural distortion could play a fundamental role in tuning the system functionality.

Materials associated with this work can be found on Materials Cloud [39].

ACKNOWLEDGMENTS

This work was supported by a Grant-in-Aid for Scientific Research on Innovative Areas "Hydrogenomics" (Grant No. JP18H05519). Numerical calculations were performed using the facility of the Supercomputer Center, Institute for Solid State Physics, University of Tokyo. We acknowledge the helpful discussions with Hidekazu Tanaka, Katsuyuki Fukutani, and Takahiro Ozawa.

APPENDIX: DISTORTION MODES

Figure 4 shows ionic distortion modes for the $SmNiO_3$ supercell. The X_1^+ mode (interlayer breathing distortion) and R_3^+ mode (out-of-phase Jahn-Teller distortion) are responsible for the charge and orbital ordering in the 4H structure.

[1] A. Mercy, J. Bieder, J. Iniguez, and P. Ghosez, Nat. Commun. **8**, 1677 (2017).
[2] J. Varignon, M. Bibes, and A. Zunger, Nat. Commun. **10**, 1658 (2019).
[3] J. Varignon, M. N. Grisolia, J. Íñiguez, A. Barthèlèmy, and M. Bibes, npj Quantum Mater. **2**, 21 (2017).
[4] Z. Liao, N. Gauquelin, R. J. Green, K. Müller-Caspary, I. Lobato, L. Li, S. Van Aert, J. Verbeeck, M. Huijben, M. N.

Grisolia, V. Rouco, R. El Hage, J. E. Villegas, A. Mercy, M. Bibes, P. Ghosez, G. A. Sawatzky, G. Rijnders, and G. Koster, Proc. Natl. Acad. Sci. USA **115**, 9515 (2018).
[5] A. Subedi, O. E. Peil, and A. Georges, Phys. Rev. B **91**, 075128 (2015).
[6] H. Park, A. J. Millis, and C. A. Marianetti, Phys. Rev. Lett. **109**, 156402 (2012).
[7] M. Medarde, C. Dallera, M. Grioni, B. Delley, F. Vernay, J. Mesot, M. Sikora, J. A. Alonso, and M. J. Martínez-Lope, Phys. Rev. B **80**, 245105 (2009).
[8] S. H. Jo, T. Chang, I. Ebong, B. B. Bhadviya, P. Mazumder, and W. Lu, Nano Lett. **10**, 1297 (2010).
[9] J. Shi, Y. Zhou, and S. Ramanathan, Nat. Commun. **5**, 4860 (2014).
[10] S. Catalano, M. Gibert, J. Fowlie, J. Iniguez, J.-M. Triscone, and J. Kreisel, Rep. Prog. Phys. **81**, 046501 (2018).
[11] Y. Zhou, S. Lee, H. Liu, S. Ramanathan, S. Adam, X. Guan, H. Zhou, K. Ramadoss, J. Shi, M. Tsuchiya, and D. D. Fong, Nature (London) **534**, 231 (2016).
[12] J. Chen, W. Mao, B. Ge, J. Wang, X. Ke, V. Wang, Y. Wang, M. Döbeli, W. Geng, H. Matsuzaki, and J. Shi, and Y. Jiang, Nat. Commun. **10**, 694 (2019).
[13] B. Torriss, J. Margot, and M. Chaker, Sci. Rep. **7**, 40915 (2017).
[14] Y. Sun, M. Kotiuga, D. Lim, and S. Ramanathan, Proc. Natl. Acad. Sci. USA **115**, 9672 (2018).
[15] P. Yoo and P. Liao, Mol. Syst. Des. Eng. **3**, 264 (2018).
[16] P. Yoo and P. Liao, Phys. Chem. Chem. Phys. **22**, 6888 (2020).
[17] Y. Cui, J. Appl. Phys. **129**, 235107 (2021).
[18] M. Kotiuga and K. M. Rabe, Phys. Rev. Mater. **3**, 115002 (2019).
[19] J. A. Alonso, M. J. Martínez-Lope, M. T. Casais, M. A. G. Aranda, and M. T. Fernandez-Diaz, J. Am. Chem. Soc. **121**, 4754 (1999).
[20] R. Jaramillo, S. D. Ha, D. M. Silevitch, and S. Ramanathan, Nat. Phys. **10**, 304 (2014).
[21] Z. Zhang, D. Schwanz, B. Narayanan, M. Kotiuga, J. A. Dura, M. Cherukara, H. Zhou, J. W. Freeland, J. Li, R. Sutarto, F. He, C. Wu, J. Zhu, Y. Sun, K. Ramadoss, S. S. Nonnenmann, N. Yu, R. Comin, K. M. Rabe, S. K. R. S. Sankaranarayanan, and S. Ramanathan, Nature (London) **553**, 68 (2018).
[22] K. Okhotnikov, T. Charpentier, and S. Cadars, J. Cheminf. **8**, 17 (2016).
[23] P. E. Blöchl, Phys. Rev. B **50**, 17953 (1994).
[24] G. Kresse and J. Furthmüller, Phys. Rev. B **54**, 11169 (1996).
[25] J. P. Perdew, K. Burke, and M. Ernzerhof, Phys. Rev. Lett. **77**, 3865 (1996).
[26] S. L. Dudarev, G. A. Botton, S. Y. Savrasov, C. J. Humphreys, and A. P. Sutton, Phys. Rev. B **57**, 1505 (1998).
[27] P. E. Blöchl, O. Jepsen, and O. K. Andersen, Phys. Rev. B **49**, 16223 (1994).
[28] See Supplemental Material at http://link.aps.org/supplemental/10.1103/PhysRevB.108.045108 for examples of the generated structure, the effect of lattice relaxation, the phonon energy contribution, the thermodynamics of hydrogen in H_x-$SmNiO_3$, hydrogen doping for apical and side oxygen sites, magnetic stability, and the effect of magnetic configurations of the electronic state. The Supplemental Material also contains Refs. [2,38,40,41].
[29] H. T. Stokes, D. M. Hatch, and B. J. Campbell, ISOCIF, ISOTROPY software suite, https://iso.byu.edu.
[30] B. J. Campbell, D. M. Hatch, and B. J. Campbell, ISODISTORT, ISOTROPY software suite, https://iso.byu.edu; B. J. Campbell, H. T. Stokes, D. E. Tanner, and D. M. Hatch, J. Appl. Crystallogr. **39**, 607 (2006).
[31] K. Momma and F. Izumi, J. Appl. Crystallogr. **44**, 1272 (2011).
[32] J. Heyd, G. E. Scuseria, and M. Ernzerhof, J. Chem. Phys. **118**, 8207 (2003).
[33] N. Marzari and D. Vanderbilt, Phys. Rev. B **56**, 12847 (1997).
[34] I. Souza, N. Marzari, and D. Vanderbilt, Phys. Rev. B **65**, 035109 (2001).
[35] A. A. Mostofi, J. R. Yates, Y. S. Lee, I. Souza, D. Vanderbilt, and N. Marzari, Comput. Phys. Commun. **185**, 2309 (2014).
[36] T. Kimura, S. Ishihara, H. Shintani, T. Arima, K. T. Takahashi, K. Ishizaka, and Y. Tokura, Phys. Rev. B **68**, 060403(R) (2003).
[37] K. Yamauchi, F. Freimuth, S. Blügel, and S. Picozzi, Phys. Rev. B **78**, 014403 (2008).
[38] F. Zuo, P. Panda, M. Kotiuga, J. Li, M. Kang, C. Mazzoli, H. Zhou, A. Barbour, S. Wilkins, B. Narayanan, M. Cherukara, Z. Zhang, S. K. R. S. Sankaranarayanan, R. Comin, K. M. Rabe, K. Roy, and S. Ramanathan, Nat. Commun. **8**, 240 (2017).
[39] K. Yamauchi and I. Hamada, Mater. Cloud Archive **2023**, 83 (2023).
[40] A. Togo and I. Tanaka, Scr. Mater. **108**, 1 (2015).
[41] J. Hermet, F. Bottin, G. Dezanneau, and G. Geneste, Phys. Rev. B **85**, 205137 (2012).